nature catalysis

Article

https://doi.org/10.1038/s41929-024-01221-5

The structural basis of pyridoxal-5′-phosphate-dependent β-NAD-alkylating enzymes

Received: 28 July 2023

Accepted: 6 August 2024

Published online: 2 September 2024

Check for updates

Takayoshi Awakawa[1,2,3,11] ✉, Takahiro Mori[1,2,4,11], Lena Barra[1,5,11], Yusef Ahmed[6], Richiro Ushimaru[1,2], Yaojie Gao[1], Naruhiko Adachi[7,8], Toshiya Senda[7,9], Tohru Terada[2,10] ✉, Dean J. Tantillo[6] ✉ & Ikuro Abe[1,2] ✉

SbzP is a unique pyridoxal-5′-phosphate-dependent enzyme, which catalyses a [3+2] annulation between the pyridinium ring of β-nicotinamide adenine dinucleotide (β-NAD) and an electron rich β,γ-unsaturated quinonoid derived from *S*-adenosylmethionine in natural product azaindane antibiotics biosynthesis. The SbzP-mediated annulation has been proposed to be a rare tandem C–C bond formation, but its structural basis and catalytic mechanism remain largely unknown. Here we report the β-NAD-complexed structure of PseP (SbzP homologue), identified by cryo-electron microscopy. Structure-based mutagenesis, stopped-flow analysis, thermal shift and surface plasmon resonance analysis identified the important residues for the substrate binding. Molecular dynamics simulations provided insights regarding how the enzyme orients the Cγ of the unsaturated quinonoid to β-NAD. In addition, density functional theory calculations confirmed that the proposed stepwise mechanism is more likely than a pericyclization mechanism. This study provides the structural basis of a pyridoxal-5′-phosphate-dependent enzyme that catalyses nucleophilic Cγ addition and β-NAD processing in natural product biosynthesis.

Pyridoxal-5′-phosphate (PLP)-dependent enzymes are among the most versatile catalysts in many cellular metabolic pathways[1,2]. They catalyse a vast range of chemical reactions, including transamination[3], decarboxylation[4], racemization[5], epimerization[6], β/γ elimination[7,8] or addition[9–11], aldol reaction[12], Claisen condensation[13], desaturation[14,15], O_2-dependent oxidation[16,17], cyclodehydration[18] and Mannich cyclization[19]. The catalytic versatility of PLP-dependent enzymes is mainly derived from the ability of PLP to work as an electron pump[20,21]. In addition, these PLP-dependent enzymes exhibit excellent regio- and stereo-selectivities, allowing for control over product distributions of complex chemical reactions[22], including the synthesis of non-proteinogenic amino acids and chiral amine compounds[3,9,19,23,24]. The discovery of biocatalysts in this family, and the study of their mechanisms for controlling catalysis, could empower the enzymatic synthesis of thus far inaccessible bioactive compounds.

[1]Graduate School of Pharmaceutical Sciences, The University of Tokyo, Tokyo, Japan. [2]Collaborative Research Institute for Innovative Microbiology, The University of Tokyo, Tokyo, Japan. [3]RIKEN Center for Sustainable Resource Science, Saitama, Japan. [4]PRESTO, Japan Science and Technology Agency, Saitama, Japan. [5]Fachbereich Chemie, Universität Konstanz, Konstanz, Germany. [6]University of California, Davis, Davis, CA, USA. [7]Structural Biology Research Center, Institute of Materials Structure Science, High Energy Accelerator Research Organization (KEK), Ibaraki, Japan. [8]Life Science Center for Survival Dynamics, University of Tsukuba, Ibaraki, Japan. [9]Faculty of Pure and Applied Sciences, University of Tsukuba, Ibaraki, Japan. [10]Department of Biotechnology, Graduate School of Agricultural and Life Sciences, The University of Tokyo, Tokyo, Japan. [11]These authors contributed equally: Takayoshi Awakawa, Takahiro Mori, Lena Barra. ✉e-mail: takayoshi.awakawa@riken.jp; tterada@bi.a.u-tokyo.ac.jp; djtantillo@ucdavis.edu; abei@mol.f.u-tokyo.ac.jp

https://doi.org/10.1038/s41929-024-01221-5

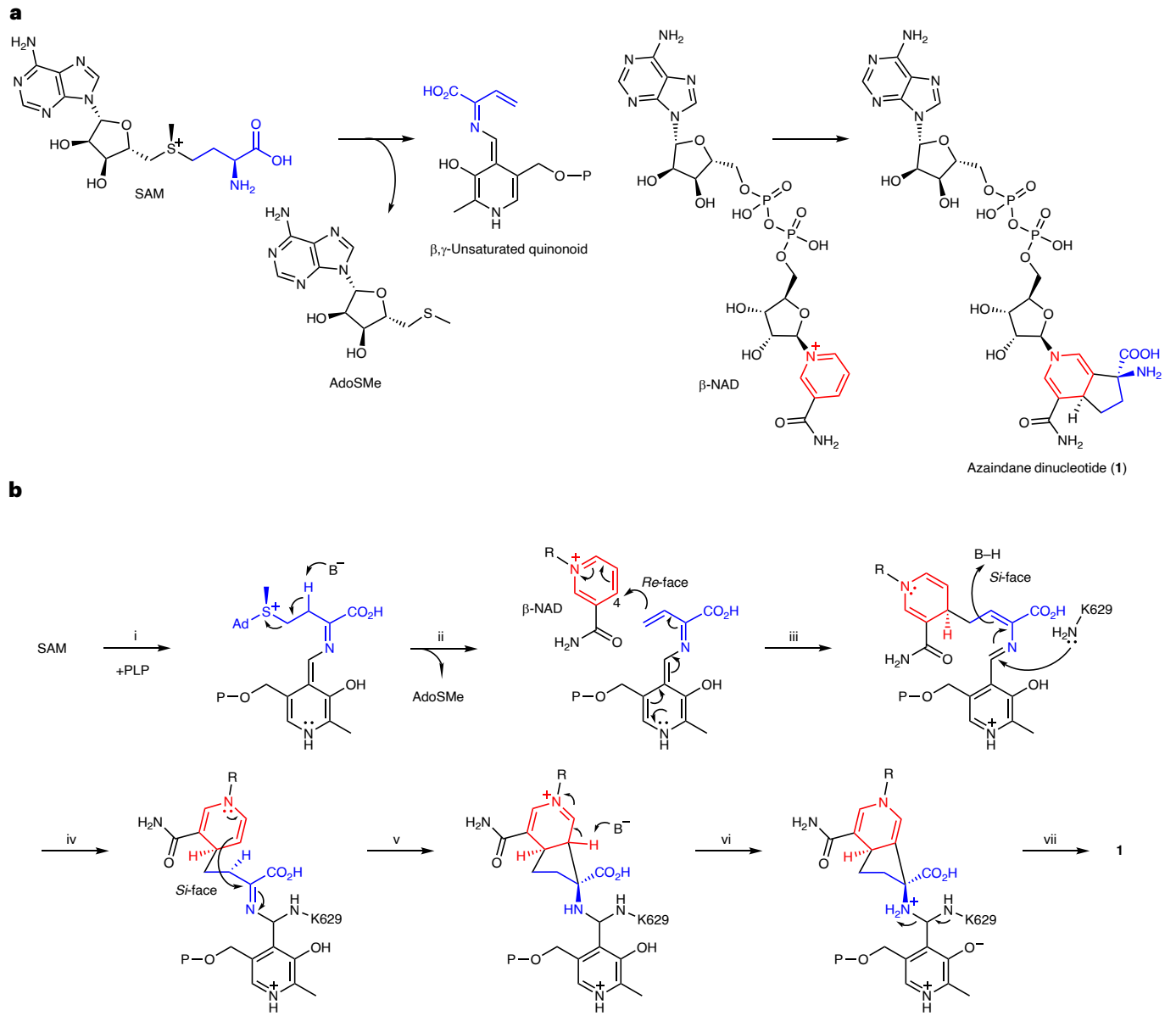

Fig. 1 | The [3+2] annulation reaction by SbzP/PseP. a, The reaction scheme of SbzP/PseP to produce 5′-methylthioadenosine (AdoSMe) and **1** from SAM and β-NAD (ref. 25). **b**, The proposed reaction mechanism: (i) SAM reacts with an internal aldimine via transaldimination, and the deprotonation at Cα generates a quinonoid species; (ii) the deprotonation at Cβ induces the elimination of AdoSMe to produce a β,γ-unsaturated quinonoid; (iii) the attack on C-4 of β-NAD by the β,γ-unsaturated quinonoid from the *re*-face generates the first C–C bond to produce intermediate I; (iv) the attack on C-4′ of intermediate I by the catalytic lysine facilitates the isomerization via reprotonation at Cβ from the *si*-face, restoring the electrophilicity of Cα and resulting in the geminal amine/imine; (v) the attack on Cα from C-5 of the dihydropyridine from the *si*-face generates the second C–C bond to produce intermediate II; (vi) the deprotonation of H-5 in intermediate II generates the dihydropyridine; and (vii) transaldimination releases the product **1**. The number of the active lysine (K629) is from PsePQ.

Recently, we identified a PLP enzyme that catalyses a [3+2] annulation between the pyridinium ring of β-NAD and the β,γ-unsaturated quinonoid derived from *S*-adenosylmethionine (SAM) to produce the azaindane dinucleotide **1**, in the biosynthesis of the actinomycetical alkaloid altemicidin (Fig. 1a)[25–27]. SbzP is the only known PLP enzyme that catalyses tandem Cγ and Cα additions and that uses the cofactor β-NAD as a substrate in natural product biosynthesis. The structural basis of this enzyme-catalysed reaction is intriguing. A Pfam database[28] search of SbzP did not assign any known β-NAD binding motifs, suggesting an unknown binding mode for the β-NAD processing. Based on the detection of a β,γ-unsaturated quinonoid in the stopped-flow analysis and the ping-pong Bi–Bi mechanism confirmed by the kinetic analysis, we proposed a reaction mechanism of SbzP (Fig. 1b)[25]: a stepwise [3+2] annulation, involving initial C–C bond formation between Cγ of the β,γ-unsaturated quinonoid and C-4 of β-NAD (dearomative pyridinium addition; step iv), followed by C–C bond formation between Cα and C-5 (step vii); a similar process was described in the recent total synthesis of altemicidin[29]. However, we could not definitively eliminate the possibility of the alternative concerted pericyclic reaction ([4+6] or [4+2] cycloaddition) between the β,γ-unsaturated quinonoid and β-NAD (Extended Data Fig. 1).

Here, based on our analysis of the cryo-electron microscopy (cryo-EM) structure of PseP (the stable SbzP homologue), coupled with structure-based mutagenesis, biophysical and computational analyses, we propose a detailed molecular mechanism for the SbzP reaction[25] and structure–function relationships for SbzP. The complex structure of PseP with β-NAD and biophysical analyses including stopped-flow analysis, thermal shift and surface plasmon resonance (SPR) analysis

https://doi.org/10.1038/s41929-024-01221-5

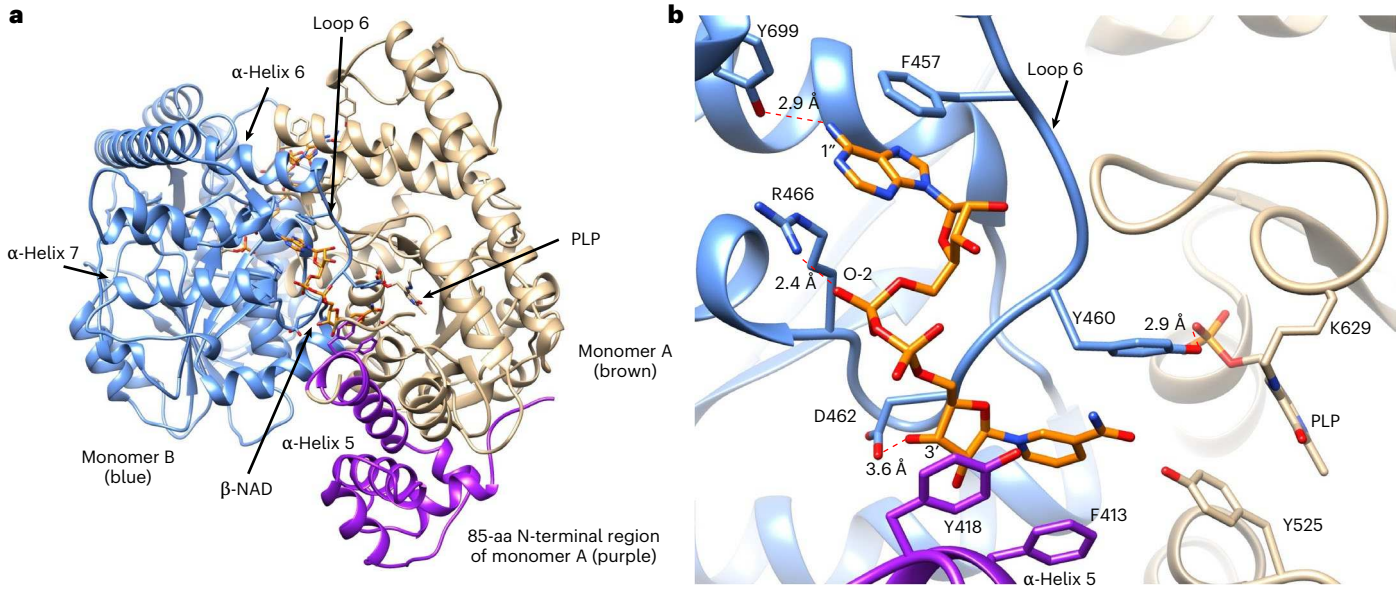

Fig. 2 | The cryo-EM structure of PsePQ complexed with β-NAD. a,**b**, The overall structure of PsePQ (**a**) and the β-NAD binding manner of PsePQ (**b**). Monomer A, monomer B, the N-terminal region of monomer A and β-NAD are coloured brown, blue, purple and orange, respectively.

show a binding mode of the PLP enzyme to the substrate β-NAD, and molecular dynamics (MD) simulations confirm that this is a possible structure in the catalytic reaction. MD simulations provide structural insights regarding how the enzyme orients the Cγ of the unsaturated quinonoid to C-4 of β-NAD. In addition, density functional theory (DFT) calculations confirm that the pericyclic reaction mechanism is unlikely, thus supporting a stepwise mechanism starting with Cγ alkylation of the quinonoid. This study provides the molecular basis of a PLP-dependent enzyme that catalyses nucleophilic Cγ alkylation to decorate the structure of the cofactor β-NAD in natural product biosynthesis.

Results

Cryo-EM structure analysis of PsePQ

For structural analysis, we used PsePQ, a chimeric protein of an SbzP homologue from *Pseudomonas* (52% amino acid identity)[25] fused to the α-ketoglutarate-dependent oxygenase PseQ, an SbzQ homologue, which catalyses the hydroxylation of **1** (Extended Data Fig. 2). PsePQ protein was purified from the *Streptomyces lividans* expression system by Ni-NTA affinity chromatography and gel filtration chromatography. Because PsePQ protein is unstable at high concentrations (>15 μM) and difficult to crystallize, we chose cryo-EM as a method for structural analysis. We spiked a PsePQ solution with several different compounds as the ligand, including β-NAD, β-NADH, SAM, *S*-adenosyl-L-homocysteine (SAH), aminovinylglycine, vinylglycine and sinefungin, and analysed the samples by single-particle cryo-EM (Supplementary Figs. 1–4 and Supplementary Tables 1 and 2). We successfully solved the structure of PsePQ without any ligand at 2.83 Å (PsePQ-apo, residues 332–811) and the structure complexed with β-NAD at 2.86 Å (PsePQ–NAD, in 20 mM β-NAD, residues 335–811; Extended Data Fig. 2 and Supplementary Table 1). The protein with SAH or SAM was also tested, but the orientation of the protein molecules was not distributed enough, leading to the failure of ab initio three-dimensional (3D) reconstruction. Thus, we were unable to obtain the 3D structure of PsePQ complexed with SAH or SAM. Although we analysed full-length PsePQ, only the 3D reconstruction of PsePQ could be established.

To biochemically characterize the PsePQ protein that we used for cryo-EM grids, we conducted sodium dodecyl-sulfate polyacrylamide gel electrophoresis (SDS-PAGE), gel filtration and size exclusion chromatography with multiple angle laser light scattering (SEC-MALS) analyses (Supplementary Figs. 5 and 6 and Extended Data Fig. 3). The SDS-PAGE analysis confirmed that the purified protein had its full length without cleavage of the PseQ region even when frozen in liquid ethane (Supplementary Fig. 5). The gel filtration profile showed that the protein had an almost identical multimerization state, and the SEC-MALS analysis showed that its molecular weight was 172.9 ± 1.2 kDa (calculated molecular weight 187.4 kDa for the dimer of N-terminal his-tagged (Nhis)–PsePQ; Supplementary Fig. 6 and Extended Data Fig. 3). These data confirmed that the PsePQ protein used for cryo-EM analysis has a dimeric structure and contains both PsePQ and PseQ. The reason why the PseQ region is not clearly observed during two-dimensional (2D) classification may be due to the variable relative positions of PsePQ and PseQ. The Alphafold2 model of PsePQ indicates that PseQ is located above α-helix 16 of PsePQ, and the 2D class average with a large mask suggests hints of supplementary density corresponding to PseQ (Extended Data Fig. 4). This density indicates a possible location of PseQ, but the data are not clear enough to determine the position. Thus, it is likely that the position is not fixed under the conditions tested in the cryo-EM experiment, as implicated by the high predicted aligned error (PAE) value of the linker region between PsePQ and PseQ (Extended Data Fig. 4).

The observed structures include the 85-aa N-terminal region (aa, amino acid), which can be aligned with the unusual N-terminal 144-aa region of SbzP. This extended N-terminal 144-aa region is not conserved in the other homologous PLP enzymes, but is essential for the activity for SbzP as shown by N-truncation experiments[25]. The overall structures form a homodimer (Fig. 2a) and are similar with type I PLP-dependent enzymes[20], in accord with the phylogenetic analysis[25]. A homology search with the DALI server revealed that the PsePQ-apo and PsePQ–NAD structures are most similar to the PLP-dependent transaminases from *Eubacterium rectale* (Protein Data Bank (PDB) no. 3ELE)[30], with r.m.s.d. values of 3.1 and 3.4 Å for the 363 and 362 Cα atoms, respectively (17 and 16% amino acid sequence identities, respectively).

In the PsePQ–NAD structure, two molecules of β-NAD are located at the dimer interface and bound to the enzyme via multiple interactions with the adenosine, diphosphate and nicotinamide riboside moieties (Fig. 2a,b and Supplementary Fig. 4). No substantial conformational change was observed between the PsePQ-apo and PsePQ–NAD structures (r.m.s.d. value = 0.3 Å; Supplementary Fig. 7). The adenine is located in the other monomer, and supported by a π-stacking interaction with

https://doi.org/10.1038/s41929-024-01221-5

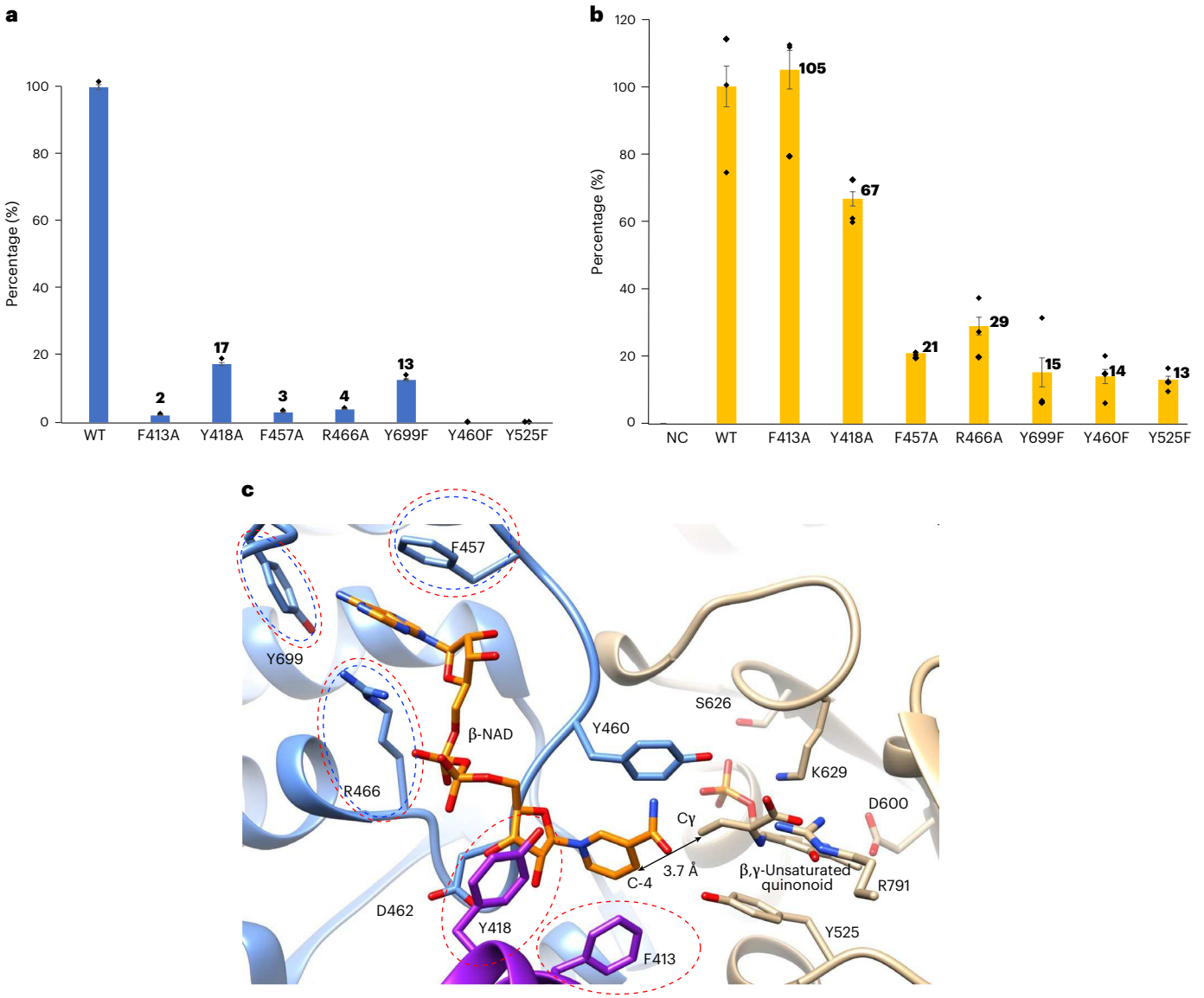

Fig. 3 | Mutagenesis analysis of PseP. a,**b**, Analysis of the relative production ratios of **1** (**a**) and AdoSMe (**b**). NC, negative control. All experiments were repeated independently three times. The bars are means of $N = 3$ independent experiments (each data point is shown by a black diamond), and error bars indicate standard deviations. **c**, The 400 ns snapshot of an MD simulation of the PseP complexed with β-NAD and β,γ-unsaturated quinonoid. Red circles indicate the residues important for ß-NAD binding, and blue circles indicate the residues important for SAM binding. The distance between Cγ of the β,γ-unsaturated quinonoid and C-4 of β-NAD is 3.7 Å.

F457 and a π–cation interaction with R466, and hydrogen bonding between Y699 and the 1″-NH_2. The adenosine ribose is supported by loop 6 between α-helices 6 and 7. The O-2 of the diphosphate is hydrogen bonded with R466. The nicotinamide riboside is accommodated within the cleft between α-helix 5 of monomer A and loop 6 of monomer B, and supported by hydrogen bonding between the 3′-OH and D462 of monomer B, the hydrophobic interaction between the ribose and Y418 of monomer A and the π-stacking interaction between the nicotinamide and F413 of monomer A. The α-helix 5, including F413 and Y418, is within the 85-aa N-terminal region, indicating the importance of this region for substrate binding (Fig. 2a,b).

Mutagenesis and biophysical analysis of PseP

To evaluate the importance of the amino acid residues that interact with β-NAD, PsePQ F413A, Y418A, F457A, R466A and Y699F variants were prepared. We could not test D462A, as it was insoluble. Y460A was constructed as a negative control, since Y460 is conserved for binding to the phosphate of PLP and the mutation ruined enzyme activity[20]. Wild-type (WT) and the variants were analysed by gel filtration, negative stain EM and SEC-MALS. The SEC-MALS analysis revealed that all the variants adopt the same dimeric structure, and the negative stain EM analysis showed that they have similar protein shape (Supplementary Figs. 6 and 8 and Extended Data Fig. 3). These data suggest that the introduced mutations do not affect the multimeric structure and the shape of the proteins. Each variant was assayed with β-NAD and SAM in the presence of PLP, and the production of **1** was analysed by liquid chromatography mass spectrometry (LC-MS). Y460F abolished the productivity of **1** by 100%; F413A, F457A and R466A decreased the activity by >95%; and Y699F and Y418A decreased the activity by >80% (Fig. 3a). These data indicate that F413, Y418, F457, R466 and Y699 are critical for the catalysis, as expected from the cryo-EM structures. To evaluate the importance of these residues for β-NAD binding, we conducted thermal shift and SPR assays. In the thermal shift assay, one of the melting temperature peaks shifted 0.9 °C and 0.5 °C upward when

β-NAD was present with WT and Y460F, respectively, but a similar shift was not detected with F413A, Y418A, F457A, R466A or Y699A (Supplementary Fig. 9). Consistently, the SPR assay showed that the WT possesses binding affinity for β-NAD (K_D = 127.7 ± 30.8 μM; K_D, dissociation constant), while the other variants lacked a comparable binding affinity (K_D > 900 μM) (Supplementary Fig. 10). These thermal shift and SPR assay data thus indicate the importance of F413, Y418, F457, R466 and Y699 for β-NAD binding (Fig. 3c). We also conducted the thermal shift assay in the presence of both SAM and β-NAD, but no additional obvious thermal shift was observed compared to that induced by β-NAD alone. Since SAM rapidly reacts with PLP to generate β,γ-unsaturated quinonoid, and the quinonoid diminishes in 5 s as shown by stopped-flow analysis[25], it is reasonable that SAM does not affect the thermal stability of the enzyme. By contrast, SAH increased the thermal stability of both the ligand-free and the β-NAD-bound enzymes (Supplementary Fig. 9). Consistent with this result, SPR experiments with 1.5 mM SAH in the running buffer showed a lower K_D value between enzyme and β-NAD compared to the data from SAH-free buffer (Supplementary Fig. 11).

To identify the residues involved in SAM binding, we constructed a docked model of PseP with SAM (Supplementary Fig. 12a). The constructed model suggested that SAM binds to the enzyme via hydrogen bonding between O-3′ and D462, a hydrophobic interaction between ribose and Y418, a cation–π interaction between the sulfonium cation and F413 and hydrogen bonding between the α-carboxyl group and R791. To verify the importance of these residues for generating the β,γ-unsaturated quinonoid, we measured the ability of these variants to produce 5′-methylthioadenosine (AdoSMe) by HPLC. F413A unexpectedly enhanced the productivity of AdoSMe by 5%, and Y418A still retained 67% of the productivity, compared with WT (Fig. 3b). These data suggest that the interactions with F413 and Y418 are not essential for SAM binding. The strong ionic interaction between F413 and the sulfonium cation may trap SAM, or F413 may also interact with AdoSMe through π-stacking with the adenine moiety, thus decreasing the turnover. By contrast, F457A, R466A and Y699F showed 21, 29 and 15% AdoSMe productivities compared to that of WT, respectively. Consistent with these biochemical analyses, in the stopped-flow analysis, the absorption at 520 nm corresponding to the β,γ-unsaturated quinonoid was only detected in WT, F413A and Y418A (Supplementary Fig. 13). The loss of the activity to generate the β,γ-unsaturated quinonoid for F457A, R466A and Y699F was unexpected, because these residues are not involved in the PLP binding site. These data suggest the possibility that SAM first binds to the adenosine binding pocket, consisting of F457A, R466A and Y699, and then transfers to the PLP binding site (Fig. 3c). Y525 is located 3.4 Å away from Cβ in the SAM-docked structure of PseP (Supplementary Fig. 12a). This residue is equivalent to Y152, which is proposed to attack the γ-position of SAM in a plant 1-aminocyclopropane-1-carboxylate synthase (ACCS)[31]. The Y525F PseP variant decreased the production of **1** and AdoSMe substantially (Fig. 3a,b), suggesting that Y525 plays a crucial role in the γ-elimination of the quinonoid. A docked model of PseP with PLP–SAM external aldimine was also constructed (Supplementary Fig. 14). In this model, the hydrogen bonding between the ribose and D462 was no longer observed, but instead the hydrogen bondings among the ribose, Y652 and S656 were observed. Y525 was located 2.5 Å away from Cβ, also suggesting its role in γ-elimination.

MD and DFT simulations of PseP reaction

To evaluate whether the position of β-NAD binding in the cryo-EM structure is reasonable for the enzyme reaction, MD simulations were performed using the positional information of β-NAD from the PseP–NAD structure and the conformation of the unsaturated quinonoid predicted from DFT calculations (Methods for details). Both ligands were docked into the enzyme and simulated for 1,000 ns trajectories. The β,γ-unsaturated quinonoid was supported via hydrogen bonding with N573, D600, S626, K629, K637 and R791, and by hydrophobic interactions with Y525 and L528 (Extended Data Fig. 5a). The distance between the Cγ of unsaturated quinonoid and the C-4 of β-NAD was maintained at less than 5.0 Å most of the time (62.1% on average) for the monomers in each calculation (Fig. 3c and Extended Data Fig. 5b–f). These data indicate that the position of β-NAD in the PseP–NAD structure likely represents the position for the reaction with the β,γ-unsaturated quinonoid. Comparing the simulated structures at 400 ns and PseP–NAD, we found that loop 6 containing F457 and R466 and loop 15 containing Y699 moved 1.9–2.0 Å and 2.8 Å upward, respectively (Supplementary Fig. 15). The position of β-NAD also moved 1.5–2.0 Å upward, suggesting that the conformational changes around the adenosine binding pocket may be important for adjusting the position of β-NAD during the enzyme reaction. R791 and K637 are conserved residues for binding to the α-carboxyl group of the substrate and the phosphate of PLP, respectively, as reported in ACCS (ref. 31) and CqsA (refs. 32,33). As expected, R791A and K637A decreased the activity to produce **1** by 82% and 100%, respectively.

To evaluate the feasibility of concerted and stepwise reaction mechanisms, DFT calculations were then conducted at the M06-2X/def2-SVP level. Concerted cycloadditions were shown to be unlikely, since these would produce an alkyl carbanion, which could not be located as a minimum on the potential energy surface (Supplementary Notes 1 and 2). The predicted energetics for the proposed reaction mechanism (Fig. 2)[25] with nucleophilic attack at C-4′ of PLP by a catalytic lysine (Supplementary Fig. 16) indicated that this mechanism was the most energetically feasible of those examined (Supplementary Figs. 16–19). In this mechanism, the two C–C bond-forming events were predicted to have small free energy barriers (13 and 4 kcal mol^{-1}). Additionally, we estimated the pK_a (where K_a is the acidity constant) of the protonated alkene to be approximately −1 (Supplementary Note 2). Although transition structures for proton transfer were not modelled explicitly, Y460 and Y525 are located close to the Cβ of SAM in the docked structure (Supplementary Fig. 12a) and are candidates for mediating proton transfer.

Discussion

We elucidated the overall and β-NAD-complexed structures of PseP. Based on these structures, mutational and computational studies provided the structural basis for the recognition of β-NAD, SAM and the β,γ-unsaturated quinonoid. In addition, results from DFT calculations suggested that the pericyclic mechanism is unlikely, and the proposed stepwise reaction mechanism[25] is plausible (Fig. 2). Notably, there are several reports on electrophilic γ-addition-catalysing PLP enzymes, such as CndF (ref. 34), Fub7 (ref. 10), FlvA (ref. 35), LolC (ref. 19) and Mur24 (ref. 11), that generate the electron-deficient vinylglycine ketimine by catalysing γ-elimination and facilitate the Michael addition of a carbon or nitrogen nucleophile at the Cγ position. This study presents the structural basis of a PLP enzyme that catalyses nucleophilic Cγ addition[36].

PseP accommodates β-NAD in the adenosine, diphosphate and nicotinamide riboside binding pockets in the active site. This mode of β-NAD binding through multiple interactions is distinct from those of the canonical NAD oxidoreductases with a Rossmann fold, in which enzymes bind β-NAD via two pairs of bidentate ribose–carboxylate interactions that occur between the side chain of Asp/Glu and the 2′-hydroxyl and 3′-hydroxyl groups of the ribose of adenosine or nicotinamide riboside[37]. In ADP-ribosyltransferase-like *Clostridium difficile* toxin[38] and poly ADP-ribose polymerase (PARP; refs. 39,40), β-NAD is also accommodated via multiple interaction sites. However, *C. difficile* toxin binds β-NAD through hydrophobic interactions and hydrogen bonds with the adenine, ribose, phosphate and nicotinamide moieties. In addition, β-NAD is folded in a conformation so the C-1 of the nicotinamide riboside can be easily attacked by a nucleophile[38], but PseP does not adopt a similar ligand conformation. PseP also recognizes β-NAD with hydrophobic interactions and hydrogen bonds via multiple sites, but it additionally employs π–π stacking with the

adenine and nicotinamide and the cleft between the two monomers. This characteristic substrate binding mode contributes to the tight substrate specificity of SbzP/PseP enzymes, which accept neither α-NAD, β-NADP nor β-nicotinamide mononucleotide (β-NMN; ref. 25).

This study elucidated the structural basis by which the PseP enzyme accommodates a β,γ-unsaturated quinonoid. Recently, McKinnie's and Ryan's groups reported the X-ray crystal structure of GntC complexed with an external aldimine[18] and Plu4 complexed with the quinonoid I, respectively[15]. In the structures of PseP, GntC and Plu4, the aldimine or quinonoid is supported by the hydrogen bonds among the α-carboxyl group, arginine (R791-PseP) and asparagine (N573-PseP); the hydrogen bonds between the amine of aldimine or the imine of quinonoid and aspartic acid (D600-PseP); and the hydrogen bonds among the phosphate, the basic residue (K637-PseP) and serine or aspartic acid (S626-PseP; Extended Data Fig. 5g,h). By contrast, the positions of the aromatic residues (Y525-PseP) and leucine (L528-PseP) vary among PLP enzymes. These differences in the hydrophobic interactions may control the reactivity.

Including SbzP/PseP, several PLP-dependent enzymes have been reported that use SAM or methylated SAM as a substrate: plant ACCS (ref. 31), bacterial ACCS GnmY (ref. 41), Orf30 (ref. 42), adenosylmethionine-8-amino-7-oxononanoate aminotransferase (DAPA; ref. 43), CqsA (refs. 32,33) and Mur24 (ref. 11). Their amino acid sequence similarities to PseP/SbzP are less than 15% (Supplementary Fig. 25a). The amino acid alignment reveals that the residues for binding to SAM or PLP–SAM external aldimine are not well conserved among them, though R791 is completely conserved, and Y460 and Y525 are partially conserved (Supplementary Fig. 25b). Among the enzymes, SbzP/PseP, CqsA and Mur24 commonly catalyse the Cγ elimination of SAM. CqsA also produces the β,γ-unsaturated quinonoid, but it catalyses nucleophilic Cα alkylation with a fatty acyl coenzyme A (acyl-CoA). Mur24 generates the quinonoid after Cα deprotonation, in common with SbzP/PseP and CqsA, but it catalyses the protonation of C-4 of the quinonoid and Cβ deprotonation, leading to the generation of a β,γ-unsaturated ketimine[11]. These three enzymes should possess a common mechanism for the Cγ elimination. We superimposed the PseP structure on the CqsA X-ray crystal structure, but the two did not fit well due to their low identity (11.9%). Thus, PseP and CqsA should use different structural bases to accommodate SAM in their active sites. By contrast, the AlphaFold2 model of Mur24 superimposed on PseP well[11,44], and the hydrogen bonds with SAM via D462 and R791 are likely to be conserved in Mur24, but not the interactions with aromatic residues corresponding to F413 and Y418 (Supplementary Fig. 12b). Comparative structural and spectral analyses of Mur24 to identify the residues required for substrate binding and the proton donor should clarify the structure–function relationships of these two enzymes[45].

In summary, we elucidated the intimate structural and mechanistic details of the PLP-dependent enzyme-catalysed nucleophilic Cγ addition reaction to generate β-NAD-derived antibiotics. We expect that these structure–function and mechanistic data will be useful for further understanding and controlling the catalysis of PLP-dependent enzymes. This information paves a way for enzyme engineering to produce β-NAD-derived and pyridinium cofactor-derived molecules[25] for future drug discovery.

Methods

General

Solvents and chemicals were purchased from Fujifilm-Wako Chemicals, Sigma-Aldrich or Kanto Chemical, unless otherwise noted. Oligonucleotide primers were purchased from Eurofins Genetics. Polymerase chain reaction (PCR) DNA amplifications were executed using a PCR Thermal Cycler Dice (TaKaRa), with Prime STAR Max DNA Polymerase (R045A, TaKaRa). Sanger DNA sequence analysis was outsourced to Eurofins Genetics to ensure that no PCR errors exist. The LC-MS analysis was conducted on a Bruker Compact qTOF mass spectrometer with a Shimadzu Prominence HPLC system.

Expression and purification of recombinant proteins

PsePQ and its mutants were expressed, and the proteins were purified from *S. lividans*/pHSA81 transformant. Because all attempts to express PsePQ in *Escherichia coli* failed, we used the high protein production system with pHSA81 in *Streptomyces*. The pHSA81 expression vector for the expression of PsePQ mutants was constructed via *E. coli* expression vector (pQTev) as described previously[25], with the primers in Supplementary Table 6. The pHSA81 expression system is based on the regulation system from nitrile hydratase (H-NHase) from *Rhodococcus rhodochrous*[46]. The incubation of the heterologous expression strain and purification of the proteins using Ni affinity and gel filtration chromatographies were carried out as described previously[25].

Cryo-EM sample preparation

The cryo-grid was prepared as described previously[47]. A 3 µl sample (6.0 µM PsePQ mixed with or without 20 mM β-NAD) was applied to a holey carbon grid (Quantifoil, Au, R1.2/1.3, 300 mesh). The grid was hydrophilized, blotted and then flash frozen in liquid ethane.

Cryo-EM data collection

For the PseP-apo dataset, a Titan Krios G3i (Thermo Fisher Scientific) microscope equipped with a Gatan Quantum-LS energy filter (slit width, 25 eV) and a Gatan K3 Summit direct electron detector in electron counting mode (CDS mode) was operated at 300 kV to acquire 6,587 videos. The electron flux at the detector was set to 7.561 e^- Å^{-2} s^{-1} where e^- is an electron. The imaging was executed at a nominal magnification of ×105,000, corresponding to a pixel size of 0.83 Å per pixel. The total electron exposure was set to 49 e^- Å^{-2}. Each video was subdivided into 1 e^- Å^{-2} per frame for all datasets. Data were automatically acquired by the image shift method using EPU software, with a defocus range of −1.0 to −1.8 µm.

For the PseP–NAD complex dataset, 3,006 videos were obtained using the same equipment as above. The electron flux at the detector was set to 8.698 e^- Å^{-2} s^{-1}. The imaging and data subdivision were performed using the same parameters as above. Data were automatically acquired by the image shift method using SerialEM software, with a defocus range of −0.8 to −1.8 µm.

Cryo-EM data processing

All the following processes were conducted using RELION (v.3.1)[48]. The data collection and refinement statistics are summarized in Supplementary Table 1. For PseP-apo datasets, dose-fractionated videos were processed as described previously[49,50]. To build 2D templates for automatic particle picking, 2,939,392 particles were selected by using template-free Laplacian-of-Gaussian picking, extracted with Laplacian-of-Gaussian picking and rescaled to 2.59375 Å per pixel with a 96-pixel box size. The extracted particle images were subjected to three rounds of reference-free 2D classification. Fine quality 2D classes (658,456 particles) were selected as templates, and 2D template-based particle picking was performed. Picked 2,771,336 particles were selected from motion-corrected micrographs with down-sampling to a pixel size of 2.59375 Å per pixel with a 96-pixel box size. These particles were subjected to the reference-free 2D classification for three cycles (first, 150 expected classes, 150 Å mask diameter; second, 50 expected classes, 135 Å mask diameter; and third, 50 expected classes, 125 Å mask diameter). After three cycles of reference-free 2D classification, 243,377 particles corresponding to the best eight classes, which displayed secondary-structural elements, were selected from the result, and then used for ab initio reconstruction (asymmetry, single expected class, 130 Å mask diameter). The 643,748 particles corresponding to the best 27 classes, which displayed secondary-structural elements, were selected for 3D classification from the second cycle of reference-free 2D classification. A C_2 symmetry was imposed on the generated ab initio map, which was used for the 3D classification (C_2 symmetry, 140 Å mask diameter). The 211,371 particles of the best 3D class, which

displayed the highest resolution, were reextracted with a pixel size of 0.83 Å per pixel with a 300-pixel box size, and subjected to auto-3D refinement (C_2 symmetry, 150 Å mask diameter). Two cycles of contrast transfer function (CTF) refinement and Bayesian polishing were performed[51]. The 3D refinement (C_2 symmetry, 120 Å mask diameter) with a soft-edged 3D mask (15-pixel extension, 30-pixel soft cosine edge) was conducted after each step of the CTF refinement and Bayesian polishing. The last 3D refinement (C_2 symmetry, 120 Å mask diameter) with a soft-edged 3D mask (15-pixel extension, 30-pixel soft cosine edge) and post-processing generated the final data at 2.83 Å resolution.

The PseP–NAD dataset was analysed in the same way as the PseP-apo dataset. To generate 2D templates for automatic particle picking, 2,059,123 particles were picked, extracted and rescaled to 4.67000 Å per pixel with a 64-pixel box size. The extracted particle images were subjected to three rounds of reference-free 2D classification. The 2D classes (250,424 particles) were selected as templates, and 2D template-based particle picking was executed. Picked 2,478,450 particles were selected from motion-corrected micrographs with down-sampling to a pixel size of 3.32 Å per pixel with a 96-pixel box size. These particles were subjected to the reference-free 2D classification for two cycles (first, 150 expected classes, 150 Å mask diameter; and second, 75 expected classes, 135 Å mask diameter). After the two cycles of reference-free 2D classification, the 574,184 particles corresponding to the best eight classes, which displayed secondary-structural elements, were selected from the result and then used for ab initio reconstruction (asymmetry, single expected class, 140 Å mask diameter). The 1,142,873 particles corresponding to the best 17 classes, which displayed secondary-structural elements, were selected for 3D classification from the second cycle of reference-free 2D classification. A C_2 symmetry was imposed on the generated ab initio map, which was used for the 3D classification (C_2 symmetry, 140 Å mask diameter). The 462,772 particles of the best 3D class, which displayed the highest resolution, were selected and reextracted with a pixel size of 0.83 Å per pixel with a 300 pixel box size, and subjected to auto-3D refinement (C_2 symmetry, 150 Å mask diameter). A cycle of CTF refinement was performed[4]. The 3D refinement (C_2 symmetry, 300 Å mask diameter) with a soft-edged 3D mask (15-pixel extension, 30-pixel soft cosine edge) was conducted after the CTF refinement step. The last 3D refinement (C_2 symmetry, 150 Å mask diameter) with a soft-edged 3D mask (15-pixel extension, 30-pixel soft cosine edge) and post-processing generated the final data at 2.86 Å resolution. A global resolution estimation with phase randomization was carried out as described previously[51–56].

For the investigation of additional densities potentially corresponding to PseQ, PseP–NAD datasets were used. Following CTFFIND4 analysis[50], 1,939,584 particles were picked by using template-free Laplacian-of-Gaussian picking (250 Å maximum diameter for the Laplacian-of-Gaussian filter) and then extracted and rescaled to 3.32 Å per pixel with a 96-pixel box size. The extracted particle images were subjected to ten rounds of reference-free 2D classification (249 Å mask diameter). The whole class of all good 2D classes were chosen in the first and second rounds. Subsequently, the best classes with additional densities potentially corresponding to PseQ were selected from the third to tenth rounds. Since substantial improvement was not observed from the fifth round, the 19,683 particles corresponding to the six classes from the fifth round of 2D classification, which displayed secondary-structural elements, were used for ab initio reconstruction (asymmetry, single expected class, 249 Å mask diameter). The models were built, modified and refined in PHENIX[57] and Coot[58].

SEC-MALS analysis

A Superdex 200 increase 10/300 GL column (Cytiva) with an Alliance 2695 system (Waters) was employed for the chromatography. PsePQ WT and its variants (0.1–0.3 µM, 100 µl) were injected into the buffer eluted at 0.5 ml min^{-1}, and the obtained data were analysed as described previously[58].

Grid preparation and data collection for negative stain EM

Proteins of PsePQ WT and its variants were diluted to 0.5 µM by buffer A (25 mM potassium phosphate (pH 7.8), 150 mM NaCl, 0.1 mM PLP). Some 4 µl of each sample was applied to a glow-discharged carbon-coated 200-mesh Cu grid (EM Japan). The sample was prepared and analysed by a JEM-1400 Plus electron microscope (JEOL) as described previously[59].

PsePQ dimer model generation by AlphaFold-Multimer

The models of the PsePQ dimer were generated using AlphaFold-Multimer[60] in ColabFold v.1.1.5 (ref. 61), and the top-ranked model was used for the analysis. For multiple sequence alignment (MSA) generations, the mmseqs2_unisref_env and unpaired_paired mode were used with default parameters. The number of recycle was 3, and relax_max_iterations was 200. The PAE plot was generated by using the generated PDB and JavaScript Object Notation (JSON) files in PAE viewer[62].

Analysis of PsePQ reaction

The mixture (50 µl) containing 2.5 µM enzyme was incubated with 0.1 mM PLP, 1.0 mM SAM and 1.0 mM β-NAD at 30 °C for 1 h in 50 mM potassium phosphate (pH 7.5). The reaction was quenched by addition of 50 µl CH_3CN, and the precipitated protein was removed by centrifugation. To check the production of **1**, the supernatant was subjected to LC-MS with a COSMOSIL 2.5 HILIC column (2.0 mm inner diameter, 100 mm length; Nacalai Tesque; solvent A, 50 mM ammonium formate (pH 9.0); solvent B, CH_3OH; solvent gradient, 100–0% B over 15 min and then 0% B isocratic over 10 min at a flow rate of 0.2 ml min^{-1}; negative ionization mode). To check the production of AdoSMe, the supernatant was subjected to HPLC with a COSMOSIL PBr column (4.6 mm inner diameter, 250 mm length; Nacalai Tesque; solvent A, 50 mM $(CH_3COO)Na$ (pH 4.7); solvent B, CH_3CN; solvent gradient, 5–5% B over 5 min, 5–50% B over 7 min and 50–100% B over 3 min at a flow rate of 1.0 ml min^{-1}). The negative control is the extract from the incubation with boiled enzyme[25].

Protein stability analysis of PsePQ

Melting points of PsePQ were obtained using real-time monitoring of changes in the intrinsic protein fluorescence by Tycho NT.6 (NanoTemper). The capillary was loaded with 10 µl of PsePQ (10 µM) in 150 mM NaCl and 25 mM potassium phosphate, pH 7.8, with or without 1.0 mM β-NAD, and heated from 35 °C to 95 °C in 3 min overall time. The melting temperature was calculated as the inflection point of the 350 nm/330 nm intrinsic fluorescence versus temperature function.

SPR analysis of PsePQ

With β-NAD used as a ligand, and PsePQ and each mutant as an analyte, the analysis was performed on a Biacore T200 SPR system (Cytiva) at 25 °C. The 1.0 µM PsePQ proteins in 300 mM NaCl and 50 mM potassium phosphate, pH 7.8, and 0.005% Tween 20 with or without 1.5 mM SAH, were immobilized on the surface of a Sensor Chip NTA (NTA, nitrilotriacetic acid; Cytiva). Twofold increasing concentrations of β-NAD (7.8–1,000 mM) were successively injected for 1 min at a flow rate of 30 µl min^{-1}, and finally one dissociation phase was recorded for 1 min. In both settings, blank runs were recorded using buffer only. Experimental data were fitted with a heterogeneous ligand model, and K_D values were calculated using Biacore T200 Evaluation software v.3.2 (Cytiva).

Stopped-flow analysis of PsePQ

PsePQ was purified by Ni-NTA affinity chromatography as described above, and concentrated to 10 µM. The analysis was conducted as described previously[25].

MD simulations

A model of the dimeric structure of PseP complexed with β-NAD and the β,γ-unsaturated quinonoid was constructed as follows. First, the

Cα atoms of a monomer of the PseP–NAD structure were superposed on those of the corresponding monomer of the PseP-apo structure, and β-NAD species were transferred into the PseP-apo structure to generate a PseP–NAD complex model. Second, the covalent bond between the C-4′ atom of PLP and the Nζ atom of Lys629 in the model was deleted, and a 2-iminobut-3-enoic acid moiety was added to the C-4′ atom of PLP. This procedure was repeated for the other monomer. The structural modelling was performed using UCSF Chimera[55].

The model thus constructed was immersed in a cube of water with dimensions of 120 Å × 120 Å × 120 Å, and potassium ions were employed to neutralize the system using the LEaP module of AmberTools 20 (ref. 63). The ff14SB force field[64] was used for the protein and the ions. The force field parameters of β-NAD were obtained from the AMBER parameter database[65,66]. The general AMBER force field 2 (GAFF2)[67] was used for the β,γ-unsaturated quinonoid, and its atomic charges were determined using the RESP method[68] based on the electrostatic potentials calculated at the HF/6-31G(*d*) level using Gaussian 16, revision B.01 (ref. 69). The TIP3P model[70] was used for water. After energy minimization and equilibration, a production MD run was performed for 1 μs, as described previously[71–80].

DFT calculations

Various [3+2] cycloaddition pathways were investigated computationally using the Gaussian 16 program, revision C.01 (ref. 69). Geometry optimizations were performed using the M06-2X functional[81,82] along with the def2-SVP basis set[83,84]. Calculations were performed with the solvation model based on density (SMD)[80] continuum method with water (ε = 78.36; where ε is permittivity). Intrinsic reaction coordinate calculations were performed for all transition structures[85–87].

Reporting summary

Further information on research design is available in the Nature Portfolio Reporting Summary linked to this article.

Data availability

The cryo-EM density maps and the atomic coordinates for the PseP-apo and PseP–NAD determined by cryo-EM have been deposited in the Electron Microscopy Data Bank (EMDB) and PDB with accession codes EMDB 36852 and PDB 8K3I, and EMDB 36851 and 8K3H, respectively. DFT-generated structures are available from ioChem-BD at https://iochem-bd.bsc.es/browse/handle/100/305360. Source data are provided with this paper.

References

1. Walsh, C. T. & Tang, Y. *The Chemical Biology of Human Vitamins* (RSC, 2019).
2. Percudani, R. & Peracchi, A. A genomic overview of pyridoxal-phosphate-dependent enzymes. *EMBO Rep.* **4**, 850–854 (2003).
3. Savile, C. K. et al. Biocatalytic asymmetric synthesis of chiral amines from ketones applied to sitagliptin manufacture. *Science* **329**, 305–309 (2010).
4. Phillips, R. S., Poteh, P., Krajcovic, D., Miller, K. A. & Hoover, T. R. Crystal structure of D-ornithine/D-lysine decarboxylase, a stereoinverting decarboxylase: implications for substrate specificity and stereospecificity of fold III decarboxylases. *Biochemistry* **58**, 1038–1042 (2019).
5. de Chiara, C. et al. D-Cycloserine destruction by alanine racemase and the limit of irreversible inhibition. *Nat. Chem. Biol.* **16**, 686–694 (2020).
6. Li, Q. et al. Deciphering the biosynthetic origin of L-*allo*-isoleucine. *J. Am. Chem. Soc.* **138**, 408–415 (2016).
7. Phillips, R. S., Demidkina, T. V. & Faleev, N. G. Structure and mechanism of tryptophan indole-lyase and tyrosine phenol-lyase. *Biochim. Biophys. Acta Proteins Proteom.* **1647**, 167–172 (2003).
8. Sato, D. & Nozaki, T. Methionine gamma-lyase: the unique reaction mechanism, physiological roles, and therapeutic applications against infectious diseases and cancers. *IUBMB Life* **61**, 1019–1028 (2009).
9. Watkins-Dulaney, E., Straathof, S. & Arnold, F. Tryptophan synthase: biocatalyst extraordinaire. *ChemBioChem* **22**, 5–16 (2021).
10. Hai, Y., Chen, M., Huang, A. & Tang, Y. Biosynthesis of mycotoxin fusaric acid and application of a PLP-dependent enzyme for chemoenzymatic synthesis of substituted L-pipecolic acids. *J. Am. Chem. Soc.* **142**, 19668–19677 (2020).
11. Cui, Z. et al. Pyridoxal-5′-phosphate-dependent alkyl transfer in nucleoside antibiotic biosynthesis. *Nat. Chem. Biol.* **16**, 904–911 (2020).
12. Seebeck, F. P. & Hilvert, D. Conversion of a PLP-dependent racemase into an aldolase by a single active site mutation. *J. Am. Chem. Soc.* **125**, 10158–10159 (2003).
13. Alexeev, D. et al. The crystal structure of 8-amino-7-oxononanoate synthase: a bacterial PLP-dependent, acyl-CoA-condensing enzyme. *J. Mol. Biol.* **284**, 401–419 (1998).
14. Du, Y.-L. et al. A pyridoxal phosphate–dependent enzyme that oxidizes an unactivated carbon-carbon bond. *Nat. Chem. Biol.* **12**, 194–199 (2016).
15. Hoffarth, E. R. et al. A shared mechanistic pathway for pyridoxal phosphate–dependent arginine oxidases. *Proc. Natl Acad. Sci. USA* **118**, e2012591118 (2021).
16. Hoffarth, E. R., Rothchild, K. W. & Ryan, K. S. Emergence of oxygen- and pyridoxal phosphate-dependent reactions. *FEBS J.* **287**, 1403–1428 (2020).
17. Noguchi, T., Isogai, S., Terada, T., Nishiyama, M. & Kuzuyama, T. Cryptic oxidative transamination of hydroxynaphthoquinone in natural product biosynthesis. *J. Am. Chem. Soc.* **144**, 5435–5440 (2022).
18. Cordoza, J. L. et al. Mechanistic and structural insights into a divergent PLP-dependent L-enduracididine cyclase from a toxic cyanobacterium. *ACS Catal.* **13**, 9817–9828 (2023).
19. Gao, J. et al. A pyridoxal 5′-phosphate-dependent Mannich cyclase. *Nat. Catal.* **6**, 476–486 (2023).
20. Eliot, A. C. & Kirsch, J. F. Pyridoxal phosphate enzymes: mechanistic, structural, and evolutionary considerations. *Annu. Rev. Biochem.* **73**, 383–415 (2004).
21. Du, Y. L. & Ryan, K. S. Pyridoxal phosphate-dependent reactions in the biosynthesis of natural products. *Nat. Prod. Rep.* **36**, 430–457 (2019).
22. Rocha, J. F., Pina, A. F., Sousa, S. F. & Cerqueira, N. M. F. S. A. PLP-dependent enzymes as important biocatalysts for the pharmaceutical, chemical and food industries: a structural and mechanistic perspective. *Catal. Sci. Technol.* **9**, 4864–4876 (2019).
23. Ellis, J. M. et al. Biocatalytic synthesis of non-standard amino acids by a decarboxylative aldol reaction. *Nat. Catal.* **5**, 136–143 (2022).
24. Kimura, T., Vassilev, V. P., Shen, G. J. & Wong, C. H. Enzymatic synthesis of β-hydroxy-α-amino acids based on recombinant D- and L-threonine aldolases. *J. Am. Chem. Soc.* **119**, 11734–11742 (1997).
25. Barra, L. et al. β-NAD as a building block in natural product biosynthesis. *Nature* **600**, 754–758 (2021).
26. Hu, Z., Awakawa, T., Ma, Z. & Abe, I. Aminoacyl sulfonamide assembly in SB-203208 biosynthesis. *Nat. Commun.* **10**, 184 (2019).
27. Barra, L., Awakawa, T. & Abe, I. Noncanonical functions of enzyme cofactors as building blocks in natural product biosynthesis. *JACS Au* **2**, 1950–1963 (2022).
28. Bateman, A. et al. The Pfam protein families database. *Nucleic Acids Res.* **28**, 263–266 (2000).

29. Harmange Magnani, C. S. & Maimone, T. J. Dearomative synthetic entry into the altemicidin alkaloids. *J. Am. Chem. Soc.* **143**, 7935–7939 (2021).
30. Fleischman, N. M. et al. Molecular characterization of novel pyridoxal-5′-phosphate-dependent enzymes from the human microbiome. *Protein Sci.* **23**, 1060–1076 (2014).
31. Huai, Q. et al. Crystal structures of 1-aminocyclopropane-1-carboxylate (ACC) synthase in complex with aminoethoxyvinylglycine and pyridoxal-5′-phosphate provide new insight into catalytic mechanisms. *J. Biol. Chem.* **276**, 38210–38216 (2001).
32. Kelly, R. C. et al. The *Vibrio cholerae* quorum-sensing autoinducer CAI-1: analysis of the biosynthetic enzyme CqsA. *Nat. Chem. Biol.* **5**, 891–895 (2009).
33. Jahan, N. et al. Insights into the biosynthesis of the *Vibrio cholerae* major autoinducer CAI-1 from the crystal structure of the PLP-dependent enzyme CqsA. *J. Mol. Biol.* **392**, 763–773 (2009).
34. Chen, M., Liu, C. T. & Tang, Y. Discovery and biocatalytic application of a PLP-dependent amino acid γ-substitution enzyme that catalyzes C–C bond formation. *J. Am. Chem. Soc.* **142**, 10506–10515 (2020).
35. Abad, A. N. D. et al. Discovery and characterization of pyridoxal 5′-phosphate-dependent cycloleucine synthases. *J. Am. Chem. Soc.* **146**, 14672–14684 (2024).
36. Liu, S. et al. Molecular and structural basis for Cγ–C bond formation by PLP-dependent enzyme Fub7. *Angew. Chem. Int. Ed.* **63**, e202317161 (2024).
37. Gherardini, P. F., Ausiello, G., Russell, R. B. & Helmer-Citterich, M. Modular architecture of nucleotide-binding pockets. *Nucleic Acids Res.* **38**, 3809–3816 (2010).
38. Sundriyal, A., Roberts, A. K., Shone, C. C. & Acharya, K. R. Structural basis for substrate recognition in the enzymatic component of ADP-ribosyltransferase toxin CDTa from *Clostridium difficile*. *J. Biol. Chem.* **284**, 28713–28719 (2009).
39. Langelier, M., Adp-ribosyl, P., Planck, J. L., Roy, S. & Pascal, J. M. Structural basis for DNA damage–dependent poly(ADP-ribosyl) ation by human PARP-1. *Science* **336**, 728–733 (2012).
40. Alemasova, E. E. & Lavrik, O. I. Poly(ADP-ribosyl)ation by PARP1: reaction mechanism and regulatory proteins. *Nucleic Acids Res.* **47**, 3811–3827 (2019).
41. Xu, Z., Pan, G., Zhou, H. & Shen, B. Discovery and characterization of 1-aminocyclopropane-1-carboxylic acid synthase of bacterial origin. *J. Am. Chem. Soc.* **140**, 16957–16961 (2018).
42. Maruyama, C. et al. *C*-Methylation of *S*-adenosyl-L-methionine occurs prior to cyclopropanation in the biosynthesis of 1-amino-2-methylcyclopropanecarboxylic acid (Norcoronamic acid) in a bacterium. *Biomolecules* **10**, 775–790 (2020).
43. Mann, S. & Ploux, O. Pyridoxal-5′-phosphate-dependent enzymes involved in biotin biosynthesis: structure, reaction mechanism and inhibition. *Biochim. Biophys. Acta Proteins Proteom.* **1814**, 1459–1466 (2011).
44. Jumper, J. et al. Highly accurate protein structure prediction with AlphaFold. *Nature* **596**, 583–589 (2021).
45. Lee, Y.-H., Ren, D., Jeon, B. & Liu, H.-W. *S*-Adenosylmethionine: more than just a methyl donor. *Nat. Prod. Rep.* **40**, 1521–1549 (2023).
46. Komeda, H., Kobayashi, M. & Shimizu, S. Characterization of the gene cluster of high-molecular-mass nitrile hydratase (H-NHase) induced by its reaction product in *Rhodococcus rhodochrous* J1. *Proc. Natl Acad. Sci. USA* **93**, 4267–4272 (1996).
47. Tao, H. et al. Discovery of non-squalene triterpenes. *Nature* **606**, 414–419 (2022).
48. Zivanov, J. et al. New tools for automated high-resolution cryo-EM structure determination in RELION-3. *eLife* **7**, e42166 (2018).
49. Zheng, S. Q. et al. MotionCor2: anisotropic correction of beam-induced motion for improved cryo-electron microscopy. *Nat. Methods* **14**, 331–332 (2017).
50. Rohou, A. & Grigorieff, N. CTFFIND4: fast and accurate defocus estimation from electron micrographs. *J. Struct. Biol.* **192**, 216–221 (2015).
51. Mori, T. et al. *C*-Glycoside metabolism in the gut and in nature: identification, characterization, structural analyses and distribution of C-C bond-cleaving enzymes. *Nat. Commun.* **12**, 6294 (2021).
52. Zivanov, J., Nakane, T. & Scheres, S. H. A Bayesian approach to beam-induced motion correction in cryo-EM single-particle analysis. *IUCrJ* **6**, 5–17 (2019).
53. Rosenthal, P. B. & Henderson, R. Optimal determination of particle orientation, absolute hand, and contrast loss in single-particle electron cryomicroscopy. *J. Mol. Biol.* **333**, 721–745 (2003).
54. Scheres, S. H. & Chen, S. Prevention of overfitting in cryo-EM structure determination. *Nat. Methods* **9**, 853–854 (2012).
55. Chen, S. et al. High-resolution noise substitution to measure overfitting and validate resolution in 3D structure determination by single particle electron cryomicroscopy. *Ultramicroscopy* **135**, 24–35 (2013).
56. Pettersen, E. F. et al. UCSF Chimera—a visualization system for exploratory research and analysis. *J. Comput. Chem.* **25**, 1605–1612 (2004).
57. Adams, P. D. et al. PHENIX: a comprehensive Python-based system for macromolecular structure solution. *Acta Crystallogr. D* **66**, 213–221 (2010).
58. Hirakawa, Y. et al. Characterization of a novel type of carbonic anhydrase that acts without metal cofactors. *BMC Biol.* **19**, 105 (2021).
59. Imasaki, T. et al. CAMSAP2 organizes a γ-tubulin-independent microtubule nucleation centre through phase separation. *Elife* **11**, e77365 (2022).
60. Emsley, P. & Cowtan, K. Coot: model-building tools for molecular graphics. *Acta Crystallogr. D* **60**, 2126–2132 (2004).
61. Zhu, W., Shenoy, A., Kundrotas, P. & Elofsson, A. Evaluation of AlphaFold-Multimer prediction on multi-chain protein complexes. *Bioinformatics* **39**, btad424 (2023).
62. Mirdita, M. et al. ColabFold: making protein folding accessible to all. *Nat. Methods* **19**, 679–682 (2022).
63. Elfmann, C. & Stülke, J. PAE viewer: a webserver for the interactive visualization of the predicted aligned error for multimer structure predictions and crosslinks. *Nucleic Acids Res.* **51**, W404–W410 (2023).
64. Case, D. A. et al. Amber 2020 (University of California, San Francisco, 2020).
65. Maier, J. A. et al. ff14SB: improving the accuracy of protein side chain and backbone parameters from ff99SB. *J. Chem. Theory Comput.* **11**, 3696–3713 (2015).
66. Walker, R. C., de Souza, M. M., Mercer, I. P., Gould, I. R. & Klug, D. R. Large and fast relaxations inside a protein: calculation and measurement of reorganization energies in alcohol dehydrogenase. *J. Phys. Chem. B* **106**, 11658–11665 (2002).
67. Pavelites, J. J., Gao, J., Bash, P. A. & Mackerell, A. D. Jr A molecular mechanics force field for NAD^+ NADH, and the pyrophosphate groups of nucleotides. *J. Comput. Chem.* **18**, 221–239 (1997).
68. Wang, J., Wolf, R. M., Caldwell, J. W., Kollman, P. A. & Case, D. A. Development and testing of a general Amber force field. *J. Comput. Chem.* **25**, 1157–1174 (2004).
69. Bayly, C. I., Cieplak, P., Cornell, W. & Kollman, P. A. A well-behaved electrostatic potential based method using charge restraints for deriving atomic charges: the RESP model. *J. Phys. Chem.* **97**, 10269–10280 (1993).
70. Frisch, M.J. et al. Gaussian 16 revision B.01 (Gaussian, 2016).

71. Lusiany, T. et al. Enhancement of SARS-CoV-2 infection via crosslinking of adjacent spike proteins by N-terminal domain-targeting antibodies. *Viruses* **15**, 2421 (2023).
72. Jorgensen, W. L., Chandrasekhar, J., Madura, J. D., Impey, R. W. & Klein, M. L. Comparison of simple potential functions for simulating liquid water. *J. Chem. Phys.* **79**, 926–935 (1983).
73. Bussi, G., Donadio, D. & Parrinello, M. Canonical sampling through velocity rescaling. *J. Chem. Phys.* **126**, 014101 (2007).
74. Bernetti, M. & Bussi, G. Pressure control using stochastic cell rescaling. *J. Chem. Phys.* **153**, 114107 (2020).
75. Hess, B., Bekker, H., Berendsen, H. J. C. & Fraaije, J. LINCS: a linear constraint solver for molecular simulations. *J. Comput. Chem.* **18**, 1463–1472 (1997).
76. Hess, B. P-LINCS: a parallel linear constraint solver for molecular simulation. *J. Chem. Theory Comput.* **4**, 116–122 (2008).
77. Darden, T., York, D. & Pedersen, L. Particle mesh Ewald: an *N*·log(*N*) method for Ewald sums in large systems. *J. Chem. Phys.* **98**, 10089–10092 (1993).
78. Essmann, U. et al. A smooth particle mesh Ewald method. *J. Chem. Phys.* **103**, 8577–8593 (1995).
79. Hess, B., Kutzner, C., van der Spoel, D. & Lindahl, E. GROMACS 4: algorithms for highly efficient, load-balanced, and scalable molecular simulation. *J. Chem. Theory Comput.* **4**, 435–447 (2008).
80. Vermeeren, P. et al. Pericyclic reaction benchmarks: hierarchical computations targeting CCSDT(Q)/CBS and analysis of DFT performance. *Phys. Chem. Chem. Phys.* **24**, 18028–18042 (2022).
81. Zhao, Y. & Truhlar, D. G. The M06 suite of density functionals for main group thermochemistry, thermochemical kinetics, noncovalent interactions, excited states, and transition elements: two new functionals and systematic testing of four M06-class functionals and 12 other functionals. *Theor. Chem. Acc.* **120**, 215–241 (2008).
82. Weigend, F. Accurate Coulomb-fitting basis sets for H to Rn. *Phys. Chem. Chem. Phys.* **8**, 1057–1065 (2006).
83. Weigend, F. & Ahlrichs, R. Balanced basis sets of split valence, triple zeta valence and quadruple zeta valence quality for H to Rn: design and assessment of accuracy. *Phys. Chem. Chem. Phys.* **7**, 3297–3305 (2005).
84. Marenich, A. V., Cramer, C. J. & Truhlar, D. G. Universal solvation model based on solute electron density and on a continuum model of the solvent defined by the bulk dielectric constant and atomic surface tensions. *J. Phys. Chem. B* **113**, 6378–6396 (2009).
85. Gonzalez, C. & Schlegel, H. B. Reaction path following in mass-weighted internal coordinates. *J. Phys. Chem.* **94**, 5523–5527 (1990).
86. Fukui, K. The path of chemical reactions - the IRC approach. *Acc. Chem. Res.* **14**, 363–368 (1981).
87. Maeda, S., Harabuchi, Y., Ono, Y., Taketsugu, T. & Morokuma, K. Intrinsic reaction coordinate: calculation, bifurcation, and automated search. *Int. J. Quantum Chem.* **115**, 258–269 (2015).

Acknowledgements

This work was supported by a Grant-in-Aid for Scientific Research from the Ministry of Education, Culture, Sports, Science and Technology, Japan (JSPS KAKENHI; grant nos. JP20H00490 (I.A.), JP20KK0173 (I.A.), JP20K22700 (R.U.), JP21H02636 (T.A.), JP21K18246 (I.A.), JP22H05123 (T.A.), JP22H05126 (T.T.), JP23K13847 (R.U.), JP23H02641 (T.M.) and JP23H00393 (I.A.)); the New Energy and Industrial Technology Development Organization (NEDO; grant no. JPNP20011 (I.A.)); AMED (grant nos. JP21ak0101164 and jp21am0101071-support number 1553 (I.A.)); the UTEC-UTokyo FSI Research Grant Program (R.U.); the PRESTO (grant no. JPMJPR20DA (T.M.)); ACT-X Programs (grant no. JPMJAX2013 (R.U.)); Fuji Foundation for Protein Research (T.M.); Japan Foundation for Applied Enzymology (T.M.); Yamada Science Foundation (T.A.); Nagase Science and Technology Foundation (T.A.); Chugai Foundation (T.A.); the Uehara Memorial Foundation (T.A.), and Naito Science & Engineering Foundation (T.A.); The Nakajima Foundation (T.A.); Takahashi Industrial and Economic Research Foundation (T.A.); and the Mitsubishi Foundation (T.A.). We thank Y. Sakamaki, T. Furuya and M. Kikkawa in the Graduate School of Medicine at the University of Tokyo for assistance with the data measurement of cryo-EM; S. Matsuoka and M. Yoshida at Advanced Research and Technology Platforms in Riken for assistance with the data measurement of SPR and thermal shift assays; T. Ueda in the Graduate School of Pharmaceutical Sciences at the University of Tokyo for the stopped-flow analysis; and R. Kato and M. Fujita at KEK for the SEC-MALS analysis. We also thank M. Kobayashi for providing pHSA81. D.J.T. and Y.A. thank the US National Science Foundation for support (CHE-2154083 and the ACCESS programme).

Author contributions

T.A. and I.A. conceived the idea for the study. T.A., T.M. and I.A. developed the hypothesis and designed the experiments. T.A., L.B. and Y.G. performed the biochemical experiments; T.A. performed the biophysical experiments; Y.A. and D.J.T. designed and performed the DFT calculations; and T.T. performed the MD simulations. T.A., T.M., R.U., T.T., N.A. and T.S. analysed the data. All authors discussed the results. T.A., T.M., R.U. and I.A. prepared the paper with input from all authors.

Competing interests

The authors declare no competing interests.

Additional information

Extended data is available for this paper at https://doi.org/10.1038/s41929-024-01221-5.

Supplementary information The online version contains supplementary material available at https://doi.org/10.1038/s41929-024-01221-5.

Correspondence and requests for materials should be addressed to Takayoshi Awakawa, Tohru Terada, Dean J. Tantillo or Ikuro Abe.

Peer review information *Nature Catalysis* thanks Shaun McKinnie, Yike Zou and the other, anonymous, reviewer(s) for their contribution to the peer review of this work.

https://doi.org/10.1038/s41929-024-01221-5

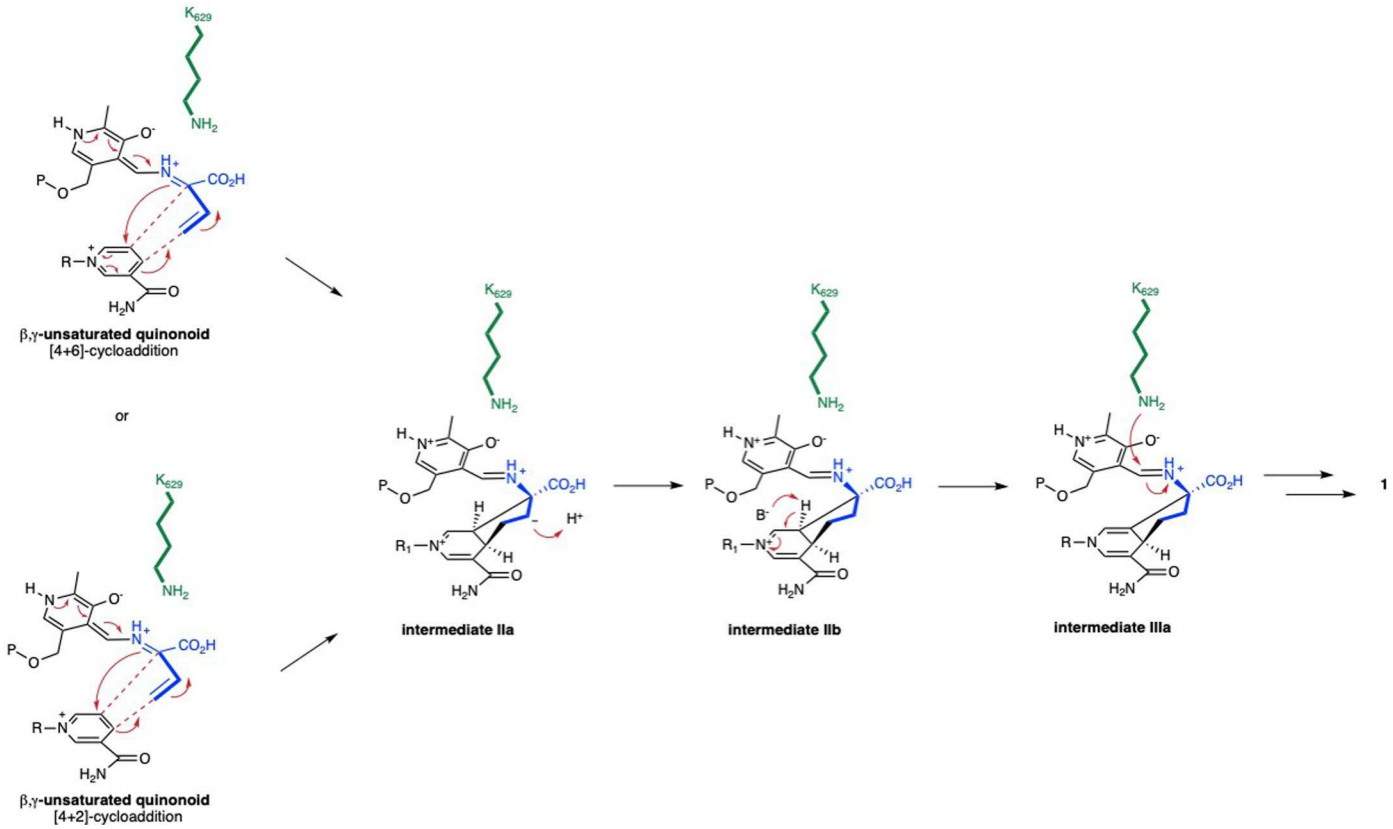

Extended Data Fig. 1 | The alternative reaction mechanism of SbzP. The alternative reaction mechanism including [4 + 6] cycloaddition or [4 + 2] cycloaddition between the β,γ-unsaturated quinonoid and β-NAD.

https://doi.org/10.1038/s41929-024-01221-5

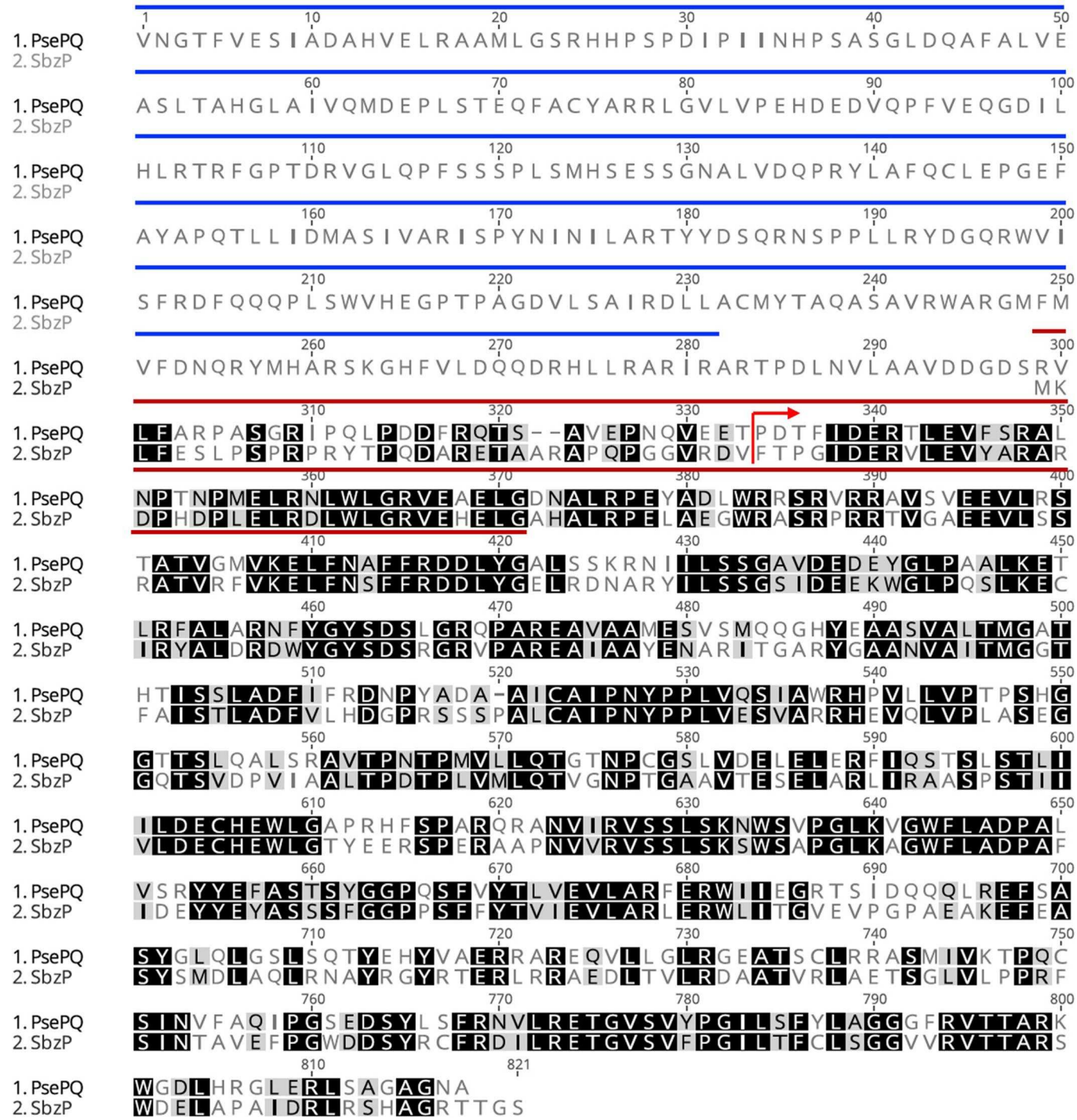

Extended Data Fig. 2 | The comparison of amino acid sequences of PsePQ and SbzP. PseQ (α-ketoglutarate dependent oxygenase)-encoding region is highlighted in blue line. The N-terminal 85 amino acid region of SbzP is highlighted in brown. The N-terminus of visible PseP-NAD structure is shown by a red arrow. The alignment was calculated with MAFFT version 7 algorithm.

https://doi.org/10.1038/s41929-024-01221-5

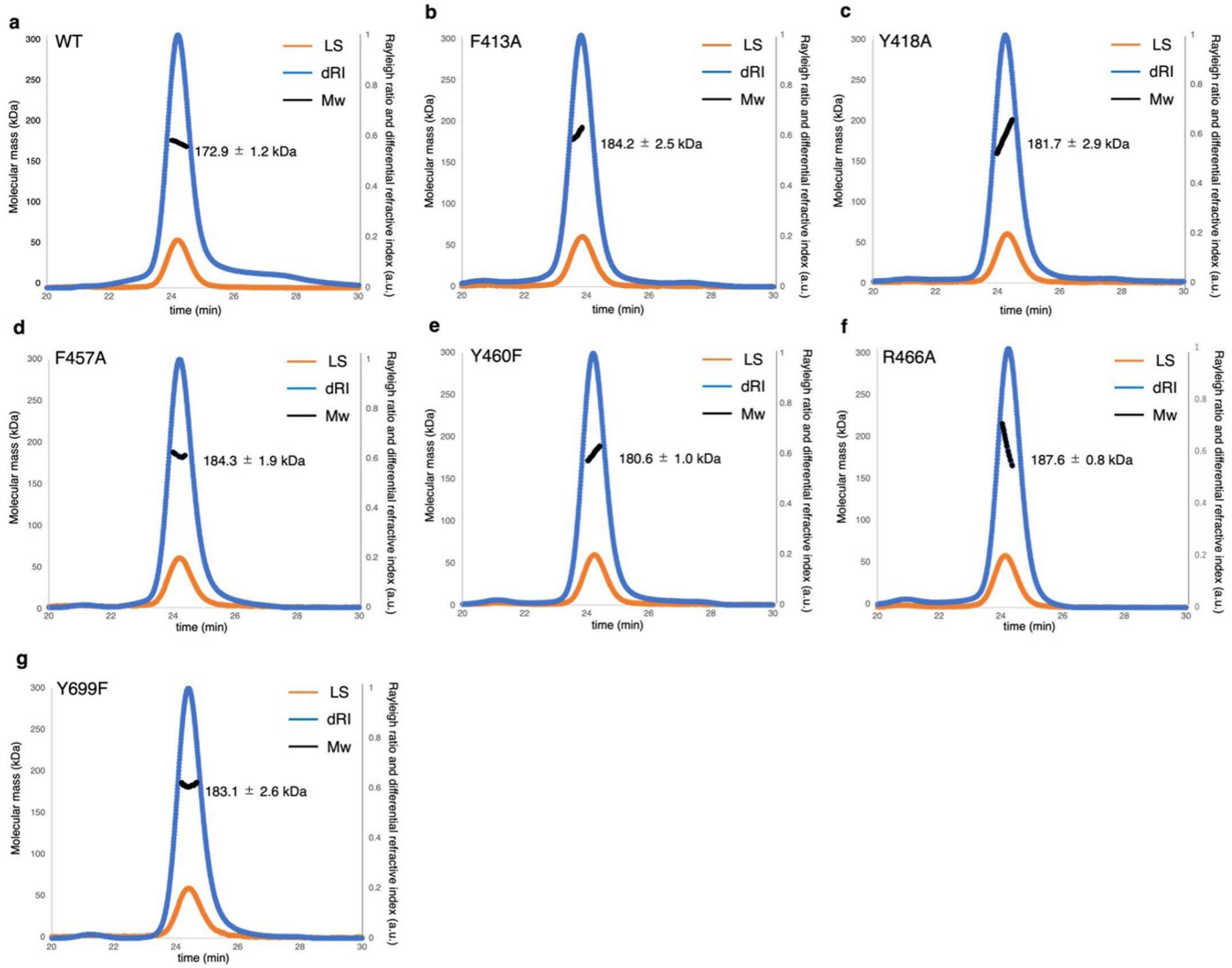

Extended Data Fig. 3 | SEC-MALS analysis of PsePQ proteins. WT (**a**) and variants (**b-g**) Light scattering (LS, orange line), differential reflective index (dRI, blue line), and the molecular weight of the protein (black line) are plotted against the elution volume. Theoretical molar mass of the Nhis-PsePQ dimer is 187.4 kDa.

https://doi.org/10.1038/s41929-024-01221-5

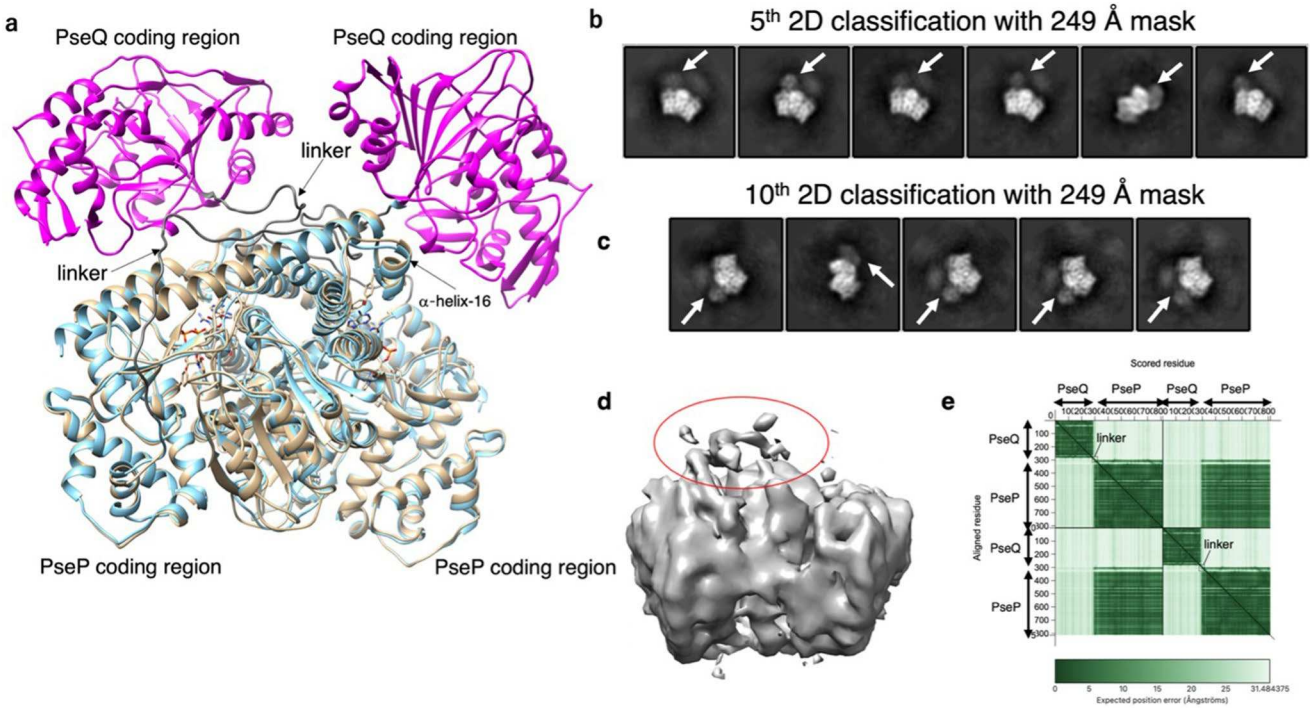

Extended Data Fig. 4 | The comparison of AlphaFold2 model with the rare view in 2D classification. (**a**) Alphafold2 model of PsePQ depicted in mazenda (PseQ), gray (linker), and cyan (PseP) overlaid by NAD-complexed cryo-EM structure. (**b**) The selected class averages from 5th round of 2D classification and (**c**) 10th round of 2D classification. (**d**) The ab-initio model of PsePQ cryo-EM structure generated using the selected class averages from 5th round of 2D classification with 249 Å of mask. The 2D classes with red squares in 5th 2D classification were used for ab-initio 3D reconstruction. The white arrow shows the structure corresponding PseQ region in the Alphafold2 model of PsePQ. (**e**) The PAE plot of PsePQ dimer Alphafold2 model generated in PAE viewer.

https://doi.org/10.1038/s41929-024-01221-5

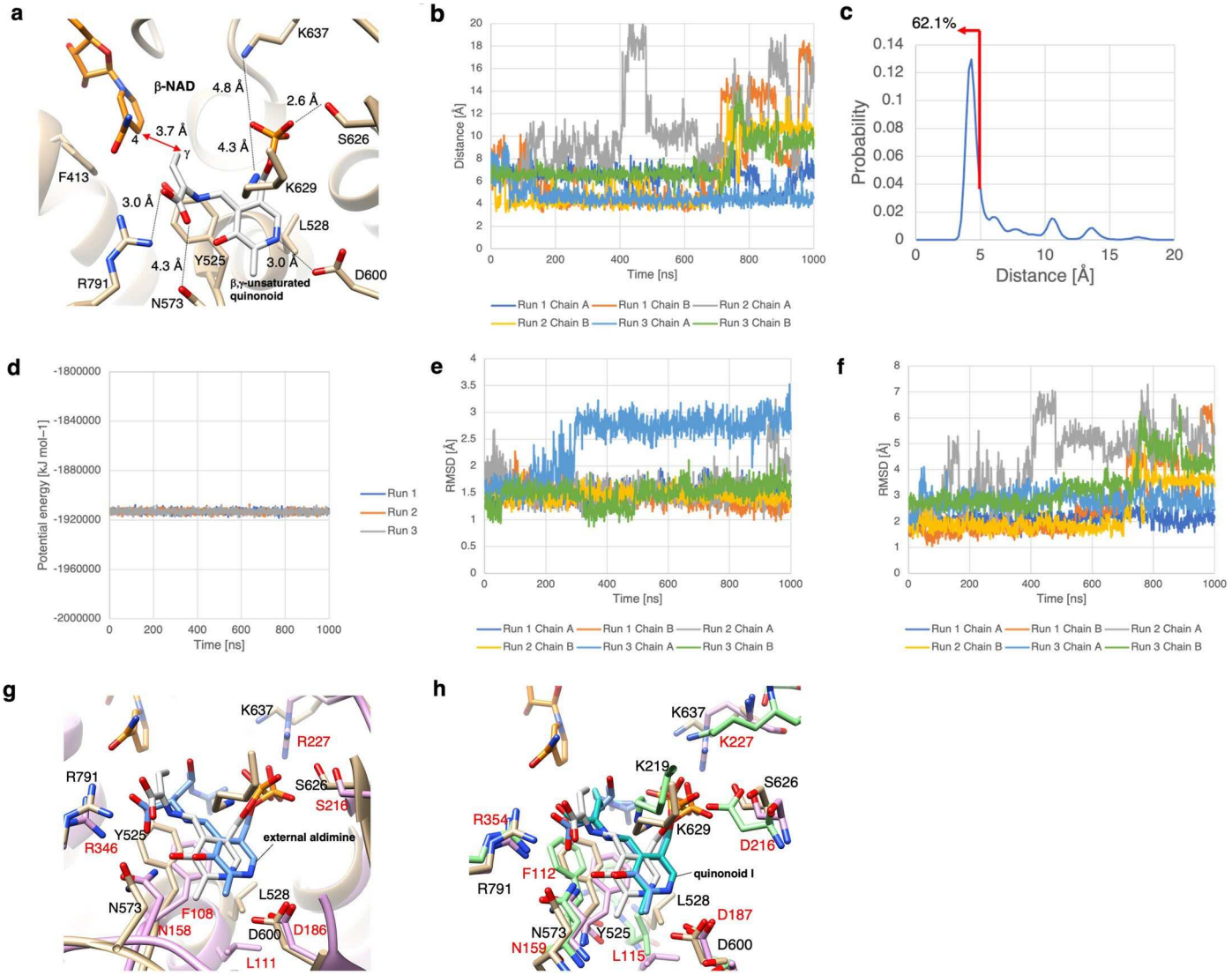

Extended Data Fig. 5 | The MD simulation of PseP and the overlay analysis of the X-ray structures of the reported PLP-dependent enzymes. (**a**) The 400 ns snapshot of apo-PseP (chain B, brown) complexed with β-NAD based on the ligand coordinate of PseP-NAD and the β,γ-unsaturated quinonoid (white) in MD simulation. (**b**) The trajectories of the distance between Cγ of the unsaturated quinonoid and C4 of β-NAD for three-different replica with different initial speeds. (**c**) Probability distribution of the distance between Cγ of the unsaturated quinonoid and C4 of β-NAD for Run 1 Chain B, Run 2 Chain B, and Run 3 Chain A. (**d**) Potential energy against simulation time for each replica. (**e**) The RMSD of the non-hydrogen atoms in β,γ-unsaturated quinonoid against simulation time. (**f**) The RMSD of the non-hydrogen atoms in β-NAD against simulation time. (**g**) The comparison of the structure shown in **a** and GntC[18]/external aldimine (PDB ID: 8FFU, the residues shown in red). (**h**) The comparison of the structure shown in **c** and Plu4[15]/quinonoid I (PDB ID: 7RF9, the residues shown in red).

nature research

Corresponding author(s): Takayoshi Awakawa, Tohru Terada, Dean J. Tantillo, Ikuro Abe

Last updated by author(s): Jul 1, 2024

Reporting Summary

Nature Research wishes to improve the reproducibility of the work that we publish. This form provides structure for consistency and transparency in reporting. For further information on Nature Research policies, see our Editorial Policies and the Editorial Policy Checklist.

Statistics

For all statistical analyses, confirm that the following items are present in the figure legend, table legend, main text, or Methods section.

n/a	Confirmed	
☐	☒	The exact sample size (*n*) for each experimental group/condition, given as a discrete number and unit of measurement
☐	☒	A statement on whether measurements were taken from distinct samples or whether the same sample was measured repeatedly
☒	☐	The statistical test(s) used AND whether they are one- or two-sided *Only common tests should be described solely by name; describe more complex techniques in the Methods section.*
☒	☐	A description of all covariates tested
☒	☐	A description of any assumptions or corrections, such as tests of normality and adjustment for multiple comparisons
☐	☒	A full description of the statistical parameters including central tendency (e.g. means) or other basic estimates (e.g. regression coefficient) AND variation (e.g. standard deviation) or associated estimates of uncertainty (e.g. confidence intervals)
☒	☐	For null hypothesis testing, the test statistic (e.g. *F*, *t*, *r*) with confidence intervals, effect sizes, degrees of freedom and *P* value noted *Give P values as exact values whenever suitable.*
☒	☐	For Bayesian analysis, information on the choice of priors and Markov chain Monte Carlo settings
☒	☐	For hierarchical and complex designs, identification of the appropriate level for tests and full reporting of outcomes
☒	☐	Estimates of effect sizes (e.g. Cohen's *d*, Pearson's *r*), indicating how they were calculated

Our web collection on statistics for biologists contains articles on many of the points above.

Software and code

Policy information about availability of computer code

Data collection	Titan Krios G3i EPU2 .10, SerialEM v3.7,
Data analysis	Geneious prime, Prism 9, Gaussian 16, UCSF Chimera13.1, AmberTools 20, RELION (3.1), CTFFIND4, PHENIX ver1.20.1-4487, Coot9, AlphaFold-Multimer,ColabFold v1.1.5, PAE viewer, Biacore T200 Evaluation software 3.2, ASTRA 6.1,

For manuscripts utilizing custom algorithms or software that are central to the research but not yet described in published literature, software must be made available to editors and reviewers. We strongly encourage code deposition in a community repository (e.g. GitHub). See the Nature Research guidelines for submitting code & software for further information.

Data

Policy information about availability of data

All manuscripts must include a data availability statement. This statement should provide the following information, where applicable:

- Accession codes, unique identifiers, or web links for publicly available datasets
- A list of figures that have associated raw data
- A description of any restrictions on data availability

Source data are provided with this paper. The data generated in this study are provided in the Supplementary Information/Source Data file. The cryo-EM density maps and the atomic coordinates for the PseP-apo and PseP/β-NAD determined by cryo-EM have been deposited in the Protein Data Bank with accession codes EMDB-36852 and 8K3I, and EMD-36851 and 8K3H respectively. DFT-generated structures are available from ioChem-BD at https://iochem-bd.bsc.es/browse/handle/100/305422.

Field-specific reporting

Please select the one below that is the best fit for your research. If you are not sure, read the appropriate sections before making your selection.

☒ Life sciences ☐ Behavioural & social sciences ☐ Ecological, evolutionary & environmental sciences

For a reference copy of the document with all sections, see nature.com/documents/nr-reporting-summary-flat.pdf

Life sciences study design

All studies must disclose on these points even when the disclosure is negative.

Sample size	This is a study for the biochemical, structural, and computational analyses of a enzyme from one specific bacteria. For all statistical experiments, including kinetics analysis were determined with n=3 as it is common practice in the field, exemplified in Nature, 527, 539-547 (2015) and J. Am. Chem. Soc. 141, 9964−9979 (2019).
Data exclusions	No data is excluded.
Replication	All attempts are performed independently and successfully replicated more than three times. Furthermore, the reproducibility of the assays was confirmed by including appropriate positive and negative controls.
Randomization	This is not relevant to our study because during the in vitro and structural analysis of target enzymes, the products, catalyzed reaction, and structure of enzymes were not known.
Blinding	Blinding is not relevant for this study because we use enzymatically synthesized substrates and mutant enzymes for in vitro reactions. During these analysis, the products, catalyzed reaction, and structure of enzymes were not known.

Reporting for specific materials, systems and methods

We require information from authors about some types of materials, experimental systems and methods used in many studies. Here, indicate whether each material, system or method listed is relevant to your study. If you are not sure if a list item applies to your research, read the appropriate section before selecting a response.

Materials & experimental systems

n/a	Involved in the study
☒	☐ Antibodies
☒	☐ Eukaryotic cell lines
☒	☐ Palaeontology and archaeology
☒	☐ Animals and other organisms
☒	☐ Human research participants
☒	☐ Clinical data
☒	☐ Dual use research of concern

Methods

n/a	Involved in the study
☒	☐ ChIP-seq
☒	☐ Flow cytometry
☒	☐ MRI-based neuroimaging